ChemPubSoc Europe

DOI: 10.1002/cssc.201601027

CHEMSUSCHEM Full Papers

VIP *Very Important Paper*

Improving the Performance of Formamidinium and Cesium Lead Triiodide Perovskite Solar Cells using Lead Thiocyanate Additives

Yue Yu,[a] Changlei Wang,[a] Corey R. Grice,[a] Niraj Shrestha,[a] Jing Chen,[b] Dewei Zhao,*[a] Weiqiang Liao,[a] Alexander J. Cimaroli,[a] Paul J. Roland,[a] Randy J. Ellingson,[a] and Yanfa Yan*[a]

Formamidinium lead triiodide ($FAPbI_3$) is considered as an alternative to methylammonium lead triiodide ($MAPbI_3$) because of its lower band gap and better thermal stability. However, owing to the large size of FA cations, it is difficult to synthesize high-quality $FAPbI_3$ thin films without the formation of an undesirable yellow phase. Smaller sized cations, such as MA and Cs, have been successfully used to suppress the formation of the yellow phase. Whereas FA and MA lead triiodide perovskite solar cells (PVSCs) have achieved power conversion efficiencies (PCEs) higher than 20%, the PCEs of formamidinium and cesium lead triiodide ($FA_{1-x}Cs_xPbI_3$) PVSCs have been only approximately 16.5%. Herein, we report our examination of the main factors limiting the PCEs of ($FA_{1-x}Cs_xPbI_3$) PVSCs. We find that one of the main limiting factors could be the small grain sizes (≈120 nm), which leads to relatively short carrier lifetimes. We further find that adding a small amount of lead thiocyanate [$Pb(SCN)_2$] to the precursors can enlarge the grain size of ($FA_{1-x}Cs_xPbI_3$) perovskite thin films and significantly increase carrier lifetimes. As a result, we are able to fabricate ($FA_{1-x}Cs_xPbI_3$) PVSCs with significantly improved open-circuit voltages and fill factors and, therefore, enhanced PCEs. With an optimal 0.5 mol% $Pb(SCN)_2$ additive, the average PCE is increased from 16.18±0.50 (13.45±0.78)% to 18.16±0.54 (16.86±0.63)% for planar $FA_{0.8}Cs_{0.2}PbI_3$ PVSCs if measured under reverse (forward) voltage scans. The champion cell registers a PCE of 19.57 (18.12)% if measured under a reverse (forward) voltage scan, which is comparable to that of the best-performing MA-containing planar FA-based lead halide PVSCs.

Introduction

Organic–inorganic methylammonium lead triiodide ($MAPbI_3$) perovskite solar cells (PVSCs) have drawn extensive attention owing to their unique photovoltaic properties and rapid improvements in their power conversion efficiencies (PCEs) during the last six years,[1–16] with the current record PCE of 22.1%.[17] Pure $MAPbI_3$ perovskite exhibits the following shortfalls that limit further improvements in device performance:

1) Its band gap (≈1.58 eV) is slightly higher than the optimal band gap range (1.2–1.45 eV) for single-junction solar cells as per the Shockley–Queisser limit[18]
2) It is not stable against moisture[19–21]
3) It undergoes a phase transition (from tetragonal to cubic phase) at approximately 55 °C and is not stable above 100 °C (decomposes with a final product of PbI_2).[12,22–26]

Recently, the α-phase black formamidinium lead triiodide ($FAPbI_3$) was suggested as an alternative to $MAPbI_3$ because of its smaller band gap (≈1.45 eV) and higher thermal stability (no phase transition between 25 and 150 °C).[22,27–31] However, despite these advantages, pure $FAPbI_3$ PVSCs have not achieved better PCEs than $MAPbI_3$-based PVSCs.[22,27,32] One of the reasons is that $FAPbI_3$ perovskite films often contain a small portion of a yellow δ-phase, which adversely affects the cell performance. The slightly too large Goldschmidt tolerance factor (*t*) caused by the large radius of FA^{1+} cations correlates with the observed formation of the yellow δ-phase.[33–35] Alloying with cations with smaller radii such as MA^{1+} and/or Cs^{1+} has been used to optimize the tolerance factor to suppress the formation of the undesirable yellow δ-phase. The alloying approach has successfully led to improved PCEs for FA-based lead halide PVSCs.[16,33,36–41]

It is noted that alloying FA with MA or MA plus Cs has led to PVSCs with PCEs higher than 20%: alloying of MA and FA has achieved PCEs above 19%,[40,42–45] whereas mixing MA, Cs, and FA has resulted in a PCE higher than 21%.[37] However, alloying

[a] Y. Yu, C. Wang, C. R. Grice, N. Shrestha, Dr. D. Zhao, W. Liao, A. J. Cimaroli, Dr. P. J. Roland, Prof. R. J. Ellingson, Prof. Y. Yan
Department of Physics and Astronomy
Wright Center for Photovoltaics Innovation and Commercialization
The University of Toledo
Toledo, OH 43606 (USA)
E-mail: dewei_zhao@hotmail.com
yanfa.yan@utoledo.edu

[b] Prof. J. Chen
School of Electronic Science and Engineering
Southeast University
Nanjing, 210096 (PR China)

Supporting Information and the ORCID identification number(s) for the author(s) of this article can be found under http://dx.doi.org/10.1002/cssc.201601027.

FA with only Cs has not yet achieved a similar level of success. Though $FA_{1-x}Cs_xPbI_3$ PVSCs have demonstrated higher PCEs and better stability than pure $FAPbI_3$ PVSCs, the highest PCE reported for $FA_{1-x}Cs_xPbI_3$ PVSCs is still approximately 16.5%.[33,38,39] With mixed FA/Cs cations and mixed I/Br anions, the PCE could be further improved to 18%.[16,36] The performance of PVSCs depends on many critical issues. The quality of the perovskite absorber layers, such as uniform substrate coverage, surface roughness, and grain size, plays a central role in determining the performance of the PVSCs. Yet, the key factors limiting the PCEs of $FA_{1-x}Cs_xPbI_3$ PVSCs have not been fully identified.

Herein, we report on our examination of the limiting factors for the PCEs of $FA_{1-x}Cs_xPbI_3$ PVSCs prepared by a one-step process. We find that pure $FAPbI_3$ perovskite thin films contain a small portion of the undesirable yellow δ-phase and have large grains, which results in rough surfaces. As soon as a small amount of Cs is added, the formation of the yellow δ-phase is suppressed. The grain size of $FA_{1-x}Cs_xPbI_3$ perovskite films decreases dramatically, which leads to significantly reduced surface roughness and dense films. Therefore, most $FA_{1-x}Cs_xPbI_3$ PVSCs exhibit PCEs surpassing those of $FAPbI_3$ PVSCs. However, further PCE improvement is limited by the small grain sizes, which are responsible for the short carrier lifetimes. We further find that a small amount of lead thiocyanate [$Pb(SCN)_2$] as an additive in the precursors enlarges the grain size of $FA_{1-x}Cs_xPbI_3$ perovskite thin films and increases the carrier lifetimes, which leads to significantly improved open-circuit voltage (V_{oc}) and fill factor (FF) values and, therefore, PCE. With an optimal 0.5 mol% $Pb(SCN)_2$ additive, the average PCE is increased from 16.18 ± 0.50 (13.45 ± 0.78)% to 18.16 ± 0.54 (16.86 ± 0.63)% for planar $FA_{0.8}Cs_{0.2}PbI_3$ PVSCs if measured under reverse (forward) voltage scans. The champion cell registers a PCE of 19.57 (18.12)% with an V_{oc} of 1.09 (1.05) V, a short-circuit current density (J_{sc}) of 22.25 (22.01) mA cm^{-2} and a FF of 80.85 (78.25)%. This performance is now comparable with that of the best-performing MA-containing planar FA-based lead halide PVSCs. It is noted that our PVSCs with the $Pb(SCN)_2$ additive are not hysteresis free, though the degree of hysteresis is reduced. The true PCE of a PVSC with hysteresis should be measured by using maximum power tracking (MPT).[46] However, this method has not been commonly used to measure the PCEs of perovskite solar cells, which makes comparison of MPT efficiencies not possible for $FA_{1-x}Cs_xPbI_3$ PVSCs.

Results and Discussion

We first discuss the effect of Cs alloying on the structural and optical properties of FA-based perovskites. Figure 1a shows the X-ray diffraction (XRD) patterns of $FA_{1-x}Cs_xPbI_3$ thin films on fluorine-doped tin oxide (FTO) substrates with Cs contents ranging from 0 to 30 mol% (i.e. $x=0$ to 0.3). The diffraction peak at $2\theta=11.44^\circ$ is from the hexagonal yellow δ-phase of $FAPbI_3$. For $x=0$ ($FAPbI_3$), a mixed phase of yellow and trigonal black $FAPbI_3$ α-phase is detected. The yellow $FAPbI_3$ peak starts to decrease as soon as 5 mol% Cs is added and then becomes negligible if the Cs content is further increased. This indicates more complete conversion into the black perovskite phase. This structural change is also visually observed during the synthesis of the film. The $FA_{1-x}Cs_xPbI_3$ ($x=0$, 0.05) film remains yellow before annealing and then turns to black upon annealing at approximately 150 °C. The as-deposited $FA_{1-x}Cs_xPbI_3$ ($x\geq0.1$) films turn black right after diethyl ether dripping at room temperature. This suggests that Cs substitution suppresses the formation of the yellow $FAPbI_3$ phase. The diffraction peak at $2\theta=12.68^\circ$ is the hexagonal PbI_2 phase, and the appearance of this peak in mixed perovskite has been commonly observed.[36,37] Upon increasing the Cs content, the PbI_2 peak starts to decrease and finally disappears if $x=0.3$. The diffraction peaks at 2θ values of 13.93, 19.75, 24.25, 28.07, 31.47, 40.11, and 42.67° correspond to the (101), (012), (021), (202), (211), (122), (024), and (131) lattice planes of the black $FAPbI_3$ phase, respectively. As seen in Figure 1b, the peak position for the (101) lattice plane gradually shifts to higher 2θ values as the Cs content increases, which is consistent with the decreased lattice constant upon Cs substitution of FA.

Figure 1c shows the absorbance spectra of the $FA_{1-x}Cs_xPbI_3$ thin films. As the Cs content increases, the absorption onset shifts to shorter wavelengths, which indicates increased band gaps. A similar trend is also observed in the normalized photoluminescence (PL) spectra, as shown in Figure 1d. The measured PL emission band shifts from 1.528 to 1.582 eV upon changing x from 0 to 0.3. The result shows that the blueshift is quite minor with different Cs contents and, therefore, shall not be a key factor influencing the device performance.

We further characterized the surface morphology of the $FA_{1-x}Cs_xPbI_3$ thin films by using scanning electron microscopy (SEM). As shown in Figure 2a, the $FAPbI_3$ thin films synthesized by our one-step process exhibit an average grain size larger than 1 μm. The grain size decreases significantly as soon as 5 mol% Cs is added. It continues to decrease as the Cs content continues to increase, and finally saturates at $x=0.15$, as seen from the SEM images shown in Figure S1 (Supporting Information). For comparison, the SEM image of a $FA_{1-x}Cs_xPbI_3$ ($x=0.2$) thin film is shown in Figure 2b. All $FA_{1-x}Cs_xPbI_3$ thin films exhibit full coverage throughout the substrate and consist of multiple grains. The average grain size (calculated by the software ImageJ) as a function of Cs content is shown in Figure 2c. Even with a small x value (i.e., Cs content), the average grain size of $FA_{1-x}Cs_xPbI_3$ dramatically decreases, changing from 1400 nm ($x=0$) to below 120 nm ($x=0.15$). The average grain size has no marked change with a further increase in the Cs content ($x=0.2$–0.3). We also measured the surface root-mean-square (RMS) roughness of the $FA_{1-x}Cs_xPbI_3$ thin films by using atomic force microscopy (AFM) (Figure S2). The measured RMS roughness as a function of Cs content is also shown in Figure 2c. It is seen that the pure $FAPbI_3$ thin film has a RMS roughness of 18 nm. Upon increasing the Cs content, the RMS roughness of $FA_{1-x}Cs_xPbI_3$ thin films first decreases, then reaches a minimum value of 5.38 nm at $x=0.2$, and then increases.

To investigate the effect of the Cs content on the device performance, planar PVSCs based on $FA_{1-x}Cs_xPbI_3$ absorbers were fabricated with the regular architecture of FTO/SnO_2/C_{60}-SAM/

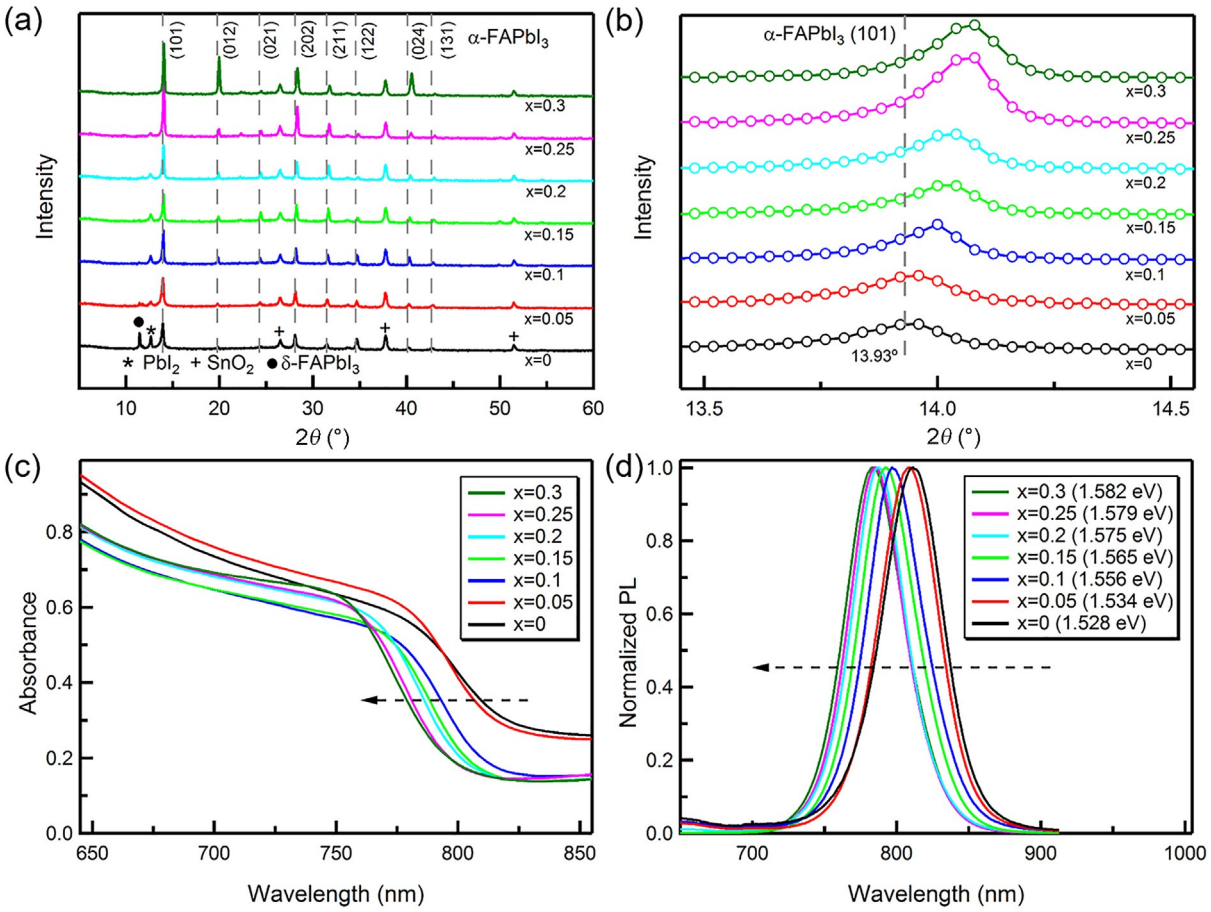

Figure 1. a) XRD patterns, b) magnified XRD patterns of the (1 0 1) lattice plane, c) absorbance spectra, and d) normalized PL spectra of $FA_{1-x}Cs_xPbI_3$ thin films with various Cs contents (*x* values).

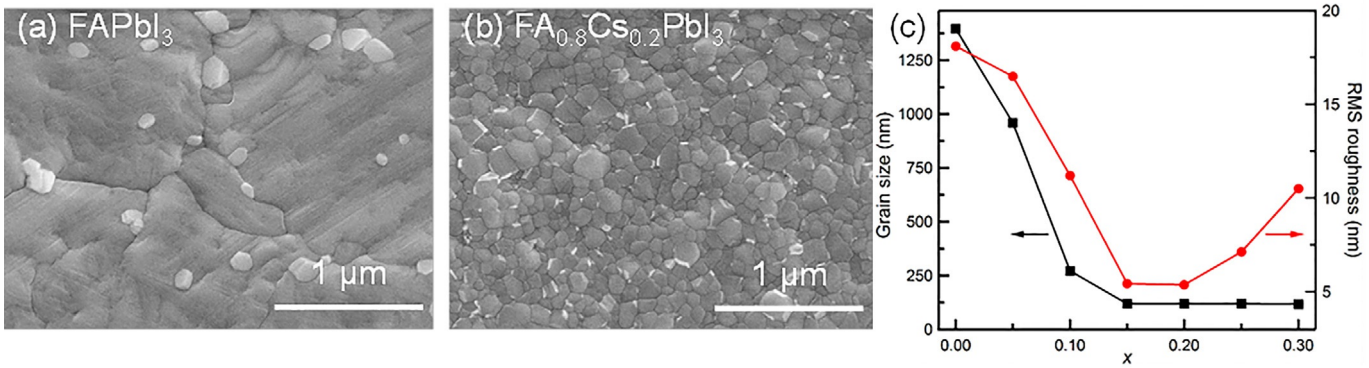

Figure 2. Top-view SEM images of a) $FAPbI_3$ and b) $FA_{0.8}Cs_{0.2}PbI_3$. c) Grain size and RMS roughness of $FA_{1-x}Cs_xPbI_3$ films as a function of the Cs content (*x* value).

$FA_{1-x}Cs_xPbI_3$/spiro-OMeTAD/Au, for which C_{60}-SAM and spiro-OMeTAD stand for fullerene and 2,2′,7,7′-tetrakis[*N*,*N*-bis(*p*-methoxyphenyl)amino]-9,9′-spirobifluorene, respectively. Figure S3 a shows the cross-sectional SEM image of a typical $FA_{1-x}Cs_xPbI_3$ PVSC. All different component layers are discrete and are clearly observed in the image. We used SnO_2 electron selective layers (ESLs). As reported previously, SnO_2 ESLs can be prepared by either a low-temperature solution process[47] or plasma-enhanced atomic layer deposition (ALD).[48] In this work, the SnO_2 ESLs were prepared by ALD. The benefits of using SnO_2 as the ESL have been discussed.[47] The proposed energy-band diagram of our PVSCs is shown in Figure S3 b.

We fabricated more than 30 cells for each Cs content. The average device performance parameters of the $FA_{1-x}Cs_xPbI_3$

PVSCs are summarized in Table S1. The pure $FAPbI_3$ PVSC shows rather low performance and gives an average PCE of 12.31 ± 1.42 (11.31 ± 1.54) % with an average V_{oc} value of 0.94 ± 0.03 (0.90 ± 0.04) V and J_{sc} value of 22.42 ± 0.93 (22.46 ± 0.80) mA cm^{-2} if measured under reverse (forward) voltage scans. Adding Cs leads to an immediate increase in cell performance. As the Cs content x increases, the PCE first increases, reaches a maximum value at $x = 0.2$, and then decreases. At $x = 0.2$, the average PCE is 16.18 ± 0.50 (13.45 ± 0.78) % with an V_{oc} of 1.03 ± 0.02 (0.97 ± 0.02) V, a J_{sc} of 21.73 ± 0.51 (21.51 ± 0.60) mA cm^{-2}, and a FF of 72.37 ± 1.18 (64.42 ± 1.71) %. It is seen that the performance improvement is mainly due to the increased values of V_{oc} and FF. The value of J_{sc} slightly decreases because of the slightly increased band gap caused by Cs substitution. The increased band gap also partially contributes to the increased value of V_{oc}. The FF increase is possibly due to the decreased surface roughness. As x further increases from 0.2 to 0.3, we observe no further improvement in V_{oc} or FF. However, the value of J_{sc} decreases further to 20.33 ± 0.34 (20.46 ± 0.53) mA cm^{-2} as a result of the increased band gap, and this leads to a decreased average PCE of 15.21 ± 0.29 (13.81 ± 0.67) % ($x = 0.3$). With our one-step process, we find that the optimal Cs content is approximately $x = 0.2$, which is close to the values reported by other groups.[16,33,36–39]

Figure 3 a shows the current density–voltage (J–V) curves of the best-performing $FAPbI_3$ and $FA_{0.8}Cs_{0.2}PbI_3$ PVSCs, with the relevant data being summarized in Table 1. The best PCE of $FAPbI_3$ is 15.18 (13.95) %, with an V_{oc} of 1.00 (0.95) V, a J_{sc} of 22.29 (22.24) mA cm^{-2}, and a FF of 68.23 (65.72) % measured under a reverse (forward) scan. The best PCE of $FA_{0.8}Cs_{0.2}PbI_3$ is 17.61 (16.19) % with an V_{oc} of 1.06 (1.00) V, a J_{sc} of 21.85 (21.90) mA cm^{-2}, and a FF of 75.94 (73.93) % measured under a reverse (forward) scan. As is consistent with the average performance parameters shown in Table S1, the values of the V_{oc} and FF of the best-performing $FA_{0.8}Cs_{0.2}PbI_3$ PVSC are higher than those of the best-performing $FAPbI_3$ PVSC, whereas the J_{sc} values are very similar. Figure 3 b shows the external quantum efficiency (EQE) spectra of the corresponding PVSCs. The integrated J_{sc} values from the EQE spectra are 21.65 mA cm^{-2} for the $FACsPbI_3$ PVSC and 21.59 mA cm^{-2} for the $FA_{0.8}Cs_{0.2}PbI_3$ PVSC, which agree well with their counterparts measured from the J–V curves. In the wavelength range of 400 to 700 nm, the EQE of the $FA_{0.8}Cs_{0.2}PbI_3$ PVSC is clearly higher than that of the $FAPbI_3$ PVSC, most likely because of the improved film quality resulting from Cs incorporation. The EQE onset edge of the $FAPbI_3$ PVSC is at a longer wavelength than that of the $FA_{0.8}Cs_{0.2}PbI_3$ PVSC owing to its smaller band gap value. Therefore the J_{sc} values of these two PVSCs are quite comparable.

Table 1. Device performance parameters of the best-performing $FAPbI_3$ and $FA_{0.8}Cs_{0.2}PbI_3$ perovskite solar cells under AM1.5G illumination at reverse and forward voltage scans.

Material	Direction	V_{oc} [V]	J_{sc} [mA cm^{-2}]	FF [%]	PCE [%]
$FAPbI_3$	reverse	1.00	22.29	68.23	15.18
	forward	0.95	22.24	65.72	13.95
$FA_{0.8}Cs_{0.2}PbI_3$	reverse	1.06	21.85	75.94	17.61
	forward	1.00	**21.90**	73.93	16.19

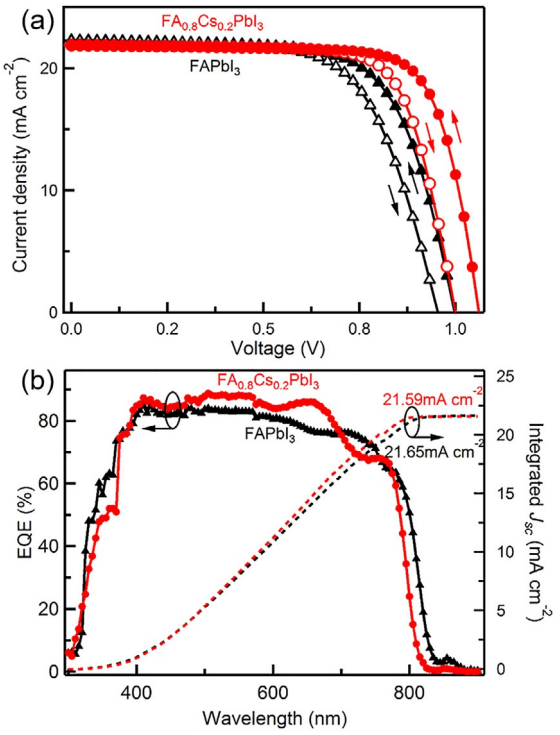

Figure 3. a) J–V curves measured under AM1.5G illumination at reverse and forward voltage scans and b) EQE spectra and integrated J_{sc} of the best-performing $FAPbI_3$ (in black) and $FA_{0.8}Cs_{0.2}PbI_3$ (in red) perovskite solar cells.

Though $FA_{0.8}Cs_{0.2}PbI_3$ PVSCs show improved cell performance relative to that shown by pure $FAPbI_3$ PVSCs, the highest PCE of 17.61 % is still much lower than the PCEs of the best PVSCs using MA-incorporated $FAPbI_3$ PVSCs. SEM images have shown that $FA_{0.8}Cs_{0.2}PbI_3$ films have small grain sizes of approximately 120 nm, which could be the factor that limits the PCEs. We have previously shown that employing $Pb(SCN)_2$ as an additive can significantly enlarge the grain size and improve the V_{oc} and FF of $MAPbI_3$ PVSCs.[49] SCN ions were initially used to improve the moisture resistance of $MAPbI_3$ perovskites.[50] However, a later investigation revealed that a high concentration SCN ions leads to the formation of the two-dimensional (2D) $MA_2Pb(SCN)_2I_2$ perovskite,[51] which is not beneficial for solar cell performance according to a recent theoretical study.[52] However, if only a small amount of $Pb(SCN)_2$ additive is added, no 2D perovskites are formed.[49] Yang et al. have recently shown that SCN ions can enlarge the grain size of pure $FAPbI_3$ thin films.[53] However, the $FAPbI_3$ PVSCs with NH_4SCN additives still cannot achieve high PCEs. Here in this work, we find that employing a small amount of $Pb(SCN)_2$ in the mixed-cation perovskite precursor solutions can enlarge the grain size and further improve the performance of $FA_{1-x}Cs_xPbI_3$ PVSCs.

To evaluate the effects of SCN ions on the performance of $FA_{1-x}Cs_xPbI_3$ PVSCs, we fixed the Cs content at $x = 0.2$, because

this Cs content gives the best cell performance, as shown in Table S1. Various $Pb(SCN)_2$ contents, ranging from 0 to 2 mol% were studied. Figure 4a shows the XRD patterns of the $FA_{0.8}Cs_{0.2}PbI_3$ thin films with various $Pb(SCN)_2$ contents in the perovskite precursor solutions. The diffraction peaks at 2θ values of 13.93, 19.75, 24.25, 28.07, 31.47, 40.11, and 42.67° corresponding to the (101), (012), (021), (202), (211), (122), (024), and (131) lattice planes of the black $FA_{0.8}Cs_{0.2}PbI_3$ phase, respectively, become stronger as the $Pb(SCN)_2$ content increases. This suggests that the grain size of the $FA_{0.8}Cs_{0.2}PbI_3$ film increases upon increasing the $Pb(SCN)_2$ content. The diffraction peak of the yellow $FAPbI_3$ phase at $2\theta = 11.44°$ is negligible in all patterns, which is due to Cs substitution, as discussed above. It is seen that the diffraction peak of PbI_2 at $2\theta = 12.68°$ increases upon increasing the content of the $Pb(SCN)_2$ additive. The trend is similar to that seen in $MAPbI_3$ and $FAPbI_3$.[49,53] As the $Pb(SCN)_2$ content is further increased to 1%, the diffraction peak of $CsPbI_3$ at $2\theta = 9.88°$ starts to appear. $CsPbI_3$ perovskite has a large band gap and is thermally unstable. The formation of this phase is highly undesirable for the performance of PVSCs. Therefore, we have limited the content of the $Pb(SCN)_2$ additive to below 2%.

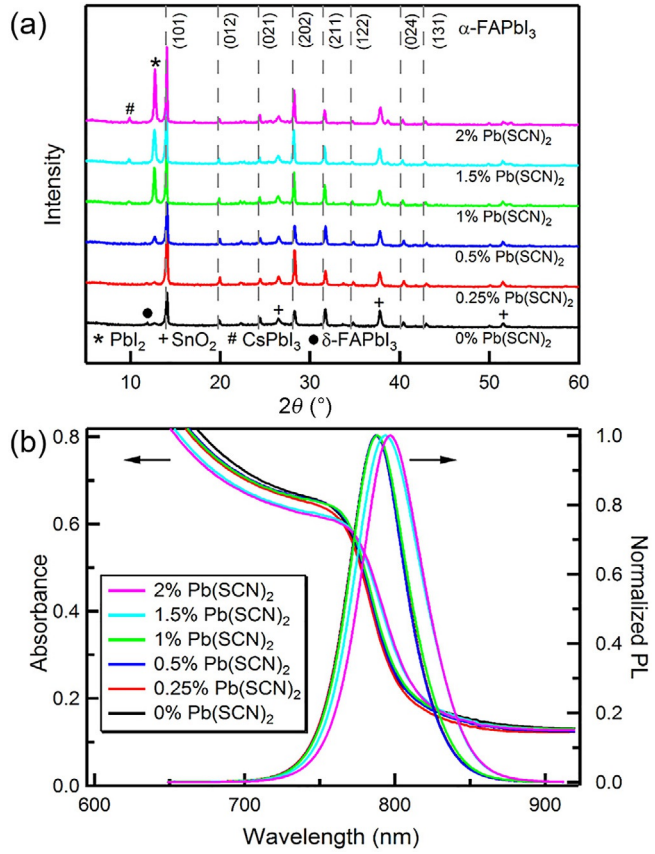

Figure 4. a) XRD patterns and b) absorbance/normalized PL spectra of $FA_{0.8}Cs_{0.2}PbI_3$ thin films with various $Pb(SCN)_2$ contents in the perovskite precursor solutions.

Figure 4b shows the absorbance and normalized PL spectra of the $FA_{0.8}Cs_{0.2}PbI_3$ thin films with various $Pb(SCN)_2$ contents. The measured PL emission bands are 1.574, 1.574, 1.574, 1.573, 1.562, 1.556 eV for the films with 0, 0.25, 0.5, 1, 1.5, and 2% $Pb(SCN)_2$ additive, respectively. For a $Pb(SCN)_2$ content below 0.5%, the PL emission band of $FA_{0.8}Cs_{0.2}PbI_3$ does not change. For $Pb(SCN)_2$ contents higher than 1%, the PL emission band of $FA_{0.8}Cs_{0.2}PbI_3$ is slightly redshifted. As shown in the above discussions, the band gap of $FA_{1-x}Cs_xPbI_3$ depends on the Cs/FA ratio, with a higher band gap observed at a higher Cs/FA ratio. Here, for a higher $Pb(SCN)_2$ concentration ($y \geq 1\%$), partial Cs is prone to form $CsPbI_3$, which leads to Cs loss in the $FA_{1-x}Cs_xPbI_3$ films. Therefore, the actual Cs content in the $FA_{0.8}Cs_{0.2}PbI_3$ films becomes lower than 0.2, which is responsible for the redshift in the PL emission band. Overall, this slight redshift should not significantly influence the device performance.

The grain size enlargement induced by the $Pb(SCN)_2$ additive is confirmed by the SEM (Figure S4) and AFM (Figure S5) images. Figure 5a,b shows the top-view SEM images of the $FA_{0.8}Cs_{0.2}PbI_3$ thin films with 0.5 and 2% $Pb(SCN)_2$ as the additive. The grain size measured from the SEM images as a function of the $Pb(SCN)_2$ amount is shown in Figure 5c. To our surprise, the grain size of $FA_{0.8}Cs_{0.2}PbI_3$ is quite sensitive to the amount of $Pb(SCN)_2$ added. For $FA_{0.8}Cs_{0.2}PbI_3$ without any $Pb(SCN)_2$, the average grain size is below 120 nm. Upon

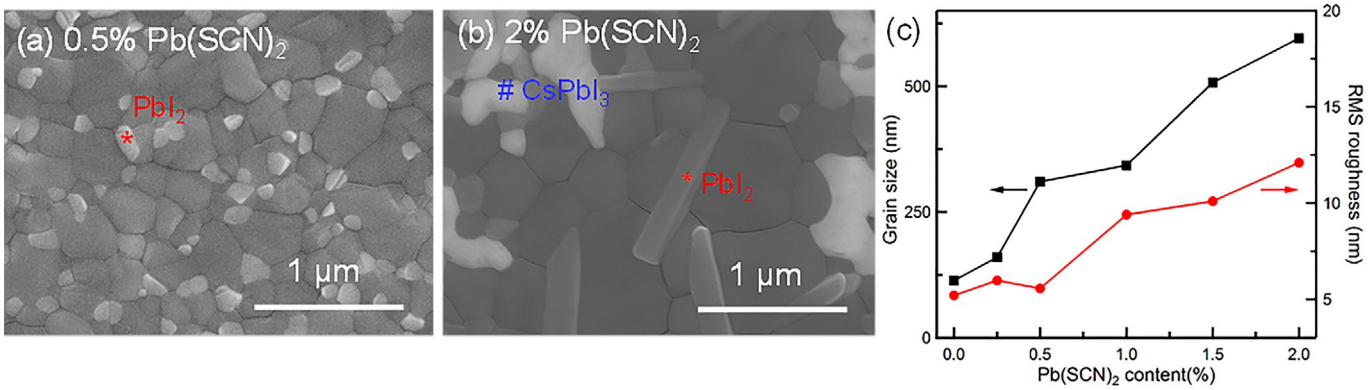

Figure 5. Top-view SEM images of $FA_{0.8}Cs_{0.2}PbI_3$ thin films with a) 0.5% and b) 2% $Pb(SCN)_2$ in the precursor solution. c) Grain size and RMS roughness of $FA_{1-x}Cs_xPbI_3$ films as a function of the $Pb(SCN)_2$ content.

adding only 0.5% $Pb(SCN)_2$, the average grain size is enlarged to 387 nm. The grain size further increases to 739 nm if 2% $Pb(SCN)_2$ is added. Consistent with the XRD results, the PbI_2 content keeps increasing as the amount of $Pb(SCN)_2$ added increases. For a lower $Pb(SCN)_2$ content (Figure 5a), PbI_2 (red marker) exhibits round-shaped grains, whereas for a higher $Pb(SCN)_2$ content (Figure 5b), large bar-shaped grains are observed. Most PbI_2 exists at the grain boundaries, which is reported to passivate the grain boundaries, and this, therefore, leads to increased PCEs.[49,54] The composition of PbI_2 is confirmed by energy-dispersive X-ray spectroscopy (EDS). Irregular-shaped $CsPbI_3$ (blue marker) grains, confirmed by EDS, are observed for a higher $Pb(SCN)_2$ content (Figure 5b). Figure S5 shows the AFM images of $FA_{0.8}Cs_{0.2}PbI_3$ thin films with various $Pb(SCN)_2$ contents, and the RMS roughness values of all six samples are shown in Figure 5c. For a lower $Pb(SCN)_2$ content ($y \leq 0.5\%$), the RMS roughness remains below 6 nm, whereas for a higher $Pb(SCN)_2$ content ($y \geq 1\%$), the RMS roughness starts to increase. As a balance of both the grain size and the surface roughness, the addition of 0.5% $Pb(SCN)_2$ might be expected for a maximum PCE.

We fabricated a large number of solar cells by using $FA_{0.8}Cs_{0.2}PbI_3$ thin films with different amounts of $Pb(SCN)_2$ as the additives. The measured device performance parameters including V_{oc}, J_{sc}, FF, and PCE are shown in Figure 6. The average device performance parameters of these PVSCs are summarized in Table S2. It is seen that the V_{oc} and the FF and, therefore, the PCE first increase, then reach maximum values at 0.5% $Pb(SCN)_2$, and then decrease. For 0.5% $Pb(SCN)_2$ additive, significant improvements in the FF and V_{oc} are observed. As a result, the average PCE improves from 16.18 ± 0.50 (13.45 ± 0.78)% to 18.16 ± 0.54 (16.86 ± 0.63)% measured under reverse (forward) voltage scans. The V_{oc} increases from 1.03 ± 0.02 (0.97 ± 0.02) V to 1.06 ± 0.01 (1.02 ± 0.02) V, the J_{sc} increases from 21.73 ± 0.51 (21.51 ± 0.60) mA cm^{-2} to 21.94 ± 0.31 (22.03 ± 0.30) mA cm^{-2}, and the FF increases from 72.37 ± 1.18 (64.42 ± 1.71)% to 77.77 ± 1.51 (75.08 ± 2.07)%. The hysteresis, defined as PCE (reverse)−PCE (forward), is also reduced from 2.7 to 1.3%. For higher $Pb(SCN)_2$ contents ($y \geq 1\%$), the PVSCs show reduced PCEs owing to the decreased V_{oc} and J_{sc} values. This trend might be attributed to the formation of the undesirable $CsPbI_3$ phase, too much PbI_2, and the increased surface roughness, even though larger $FA_{0.8}Cs_{0.2}PbI_3$ grain sizes are observed.

Figure 7a shows the *J*–*V* curves of the best-performing $FA_{0.8}Cs_{0.2}PbI_3$ PVSC with 0.5% $Pb(SCN)_2$ additive measured

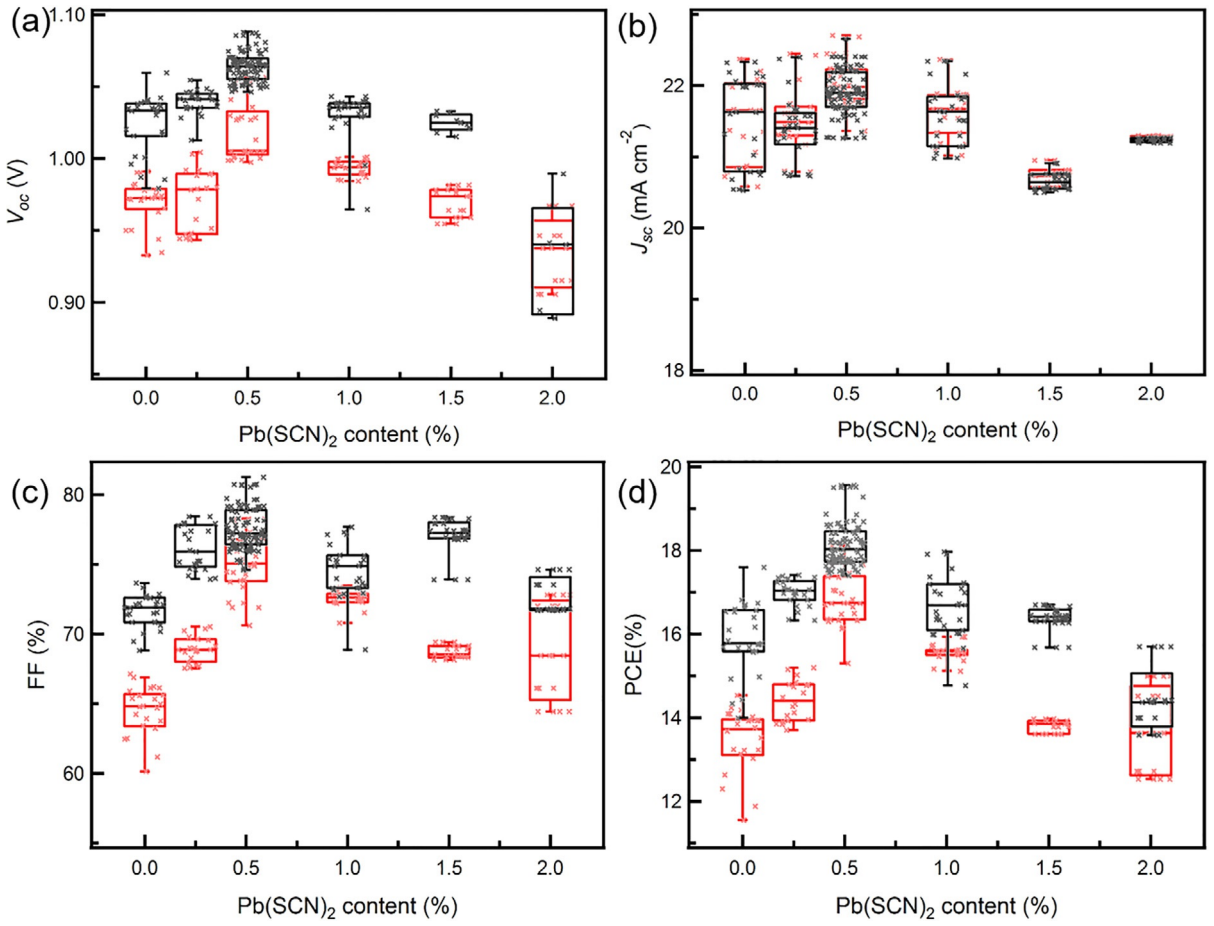

Figure 6. Device performance of $FA_{0.8}Cs_{0.2}PbI_3$ PVSCs with various $Pb(SCN)_2$ contents in the precursor. a) V_{oc}, b) J_{sc}, c) FF, and d) PCE measured under reverse (black)/forward (red) voltage scans.

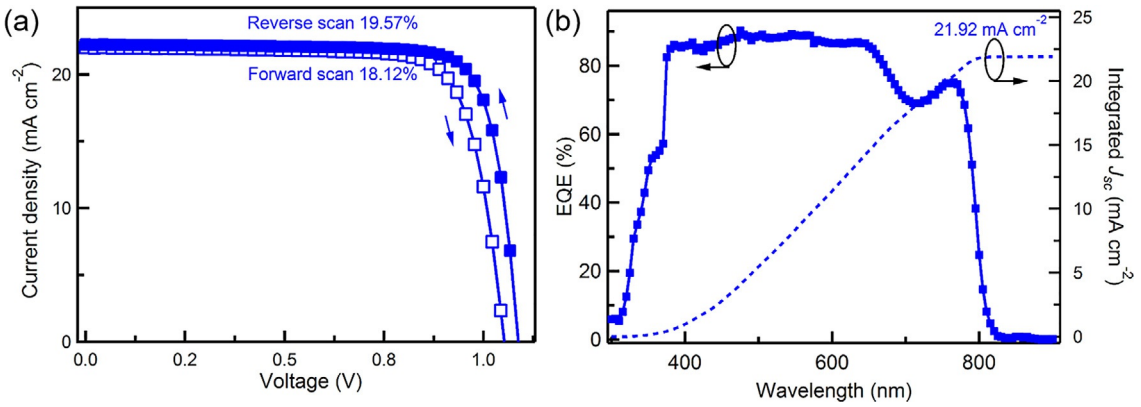

Figure 7. a) *J–V* curves measured under AM1.5G illumination at reverse and forward voltage scans and b) EQE spectrum and integrated J_{sc} of the best-performing $FA_{0.8}Cs_{0.2}PbI_3$ PVSC with 0.5% $Pb(SCN)_2$ as additive.

Table 2. Device performance parameters of the best-performing $FA_{0.8}Cs_{0.2}PbI_3$ perovskite solar cell with 0.5% $Pb(SCN)_2$ additive under AM1.5G illumination at reverse and forward voltage scans.

Direction	V_{oc} [V]	J_{sc} [mA cm^{-2}]	FF [%]	PCE [%]
reverse	1.09	22.25	80.85	19.57
forward	1.05	22.01	78.25	18.12

under AM1.5G illumination, with the data being summarized in Table 2. This cell shows a PCE of 19.57 (18.12)% with an V_{oc} of 1.09 (1.05) V, a J_{sc} of (22.25) 22.01 mA cm^{-2}, and a FF of 80.85 (78.25)% measured at a reverse (forward) scan. Figure 7b shows the EQE spectrum of the corresponding PVSC. The integrated J_{sc} value from the EQE is 21.92 mA cm^{-2}, which agrees well with the J_{sc} value obtained from the *J–V* curve. The spectrum dip at a wavelength of approximately 700 nm is possibly related to the spiro-OMeTAD we used, which is partially responsible for the current loss. A similar EQE dipping shape has also been observed elsewhere.[55,56] Optimizing the hole selective layers should lead to further PCE improvements.

To understand the mechanism of the performance improvement caused by $Pb(SCN)_2$, we conducted time-resolved photoluminescence (TRPL) measurements on the pure $FAPbI_3$ film and $FA_{0.8}Cs_{0.2}PbI_3$ films with and without 0.5% $Pb(SCN)_2$ as the additive deposited on FTO substrates. As shown in Figure 8a, the mean photogenerated carrier life time (τ_n) of the pure $FAPbI_3$ thin film is only 19 ns. The $FA_{0.8}Cs_{0.2}PbI_3$ film without the $Pb(SCN)_2$ additive in the precursor shows a longer lifetime of 31 ns, though it has smaller grains than pure $FAPbI_3$. This implies that the $FAPbI_3$ film may have a poorer film quality. The $FA_{0.8}Cs_{0.2}PbI_3$ film with 0.5% $Pb(SCN)_2$ as the additive in the precursor shows a much increased lifetime, 167 ns. We further measured the V_{oc} and J_{sc} values under different light intensities ranging from 0.5 to 100 mW cm^{-2}. The change in V_{oc} as a function of the light intensity is plotted in Figure 8b. The V_{oc} has a linear relationship with the natural logarithmic light intensity and the fitted slopes are 1.72, 1.71, and 1.55 $k_B Te^{-1}$ (k_B is the Boltzmann constant, T is the absolute temperature, and e is the electron charge) for the $FAPbI_3$, $FA_{0.8}Cs_{0.2}PbI_3$, and

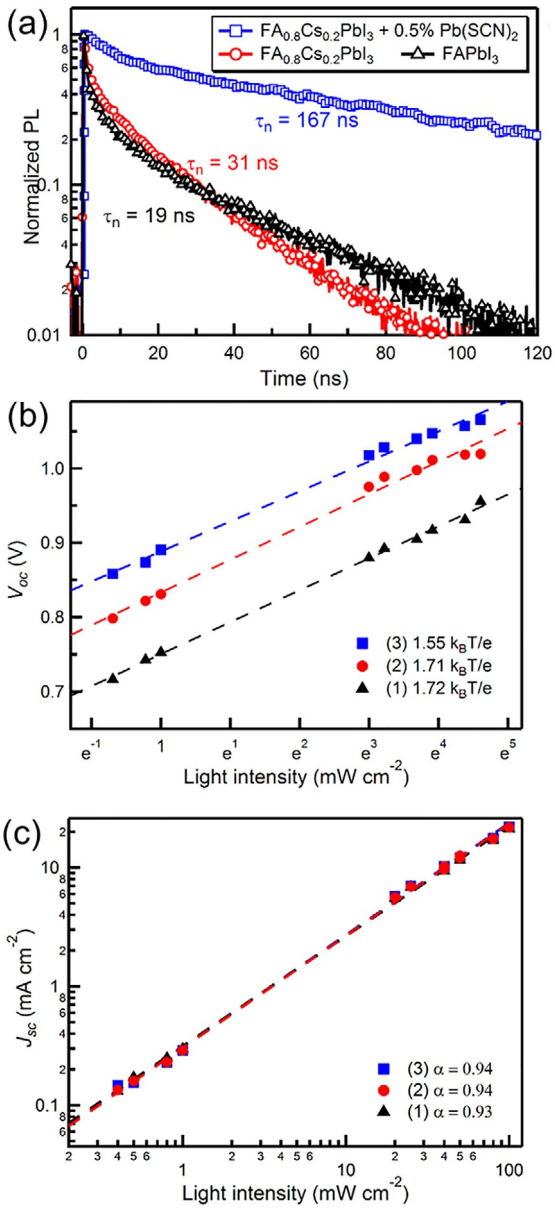

Figure 8. a) PL decay and light intensity dependence of b) V_{oc} and c) J_{sc} of $FAPbI_3$ and $FA_{0.8}Cs_{0.2}PbI_3$ films with and without 0.5% $Pb(SCN)_2$ as additive.

$FA_{0.8}Cs_{0.2}PbI_3$+0.5% $Pb(SCN)_2$ PVSCs, respectively, which indicates the presence of Shockley–Read–Hall recombination in these PVSCs.[57] The trap-assisted recombination is lower in the $FA_{0.8}Cs_{0.2}PbI_3$+0.5% $Pb(SCN)_2$ PVSC than in the $FA_{0.8}Cs_{0.2}PbI_3$ and $FA_{0.8}Cs_{0.2}PbI_3$ PVSCs. Figure 8c shows the power law dependence of the J_{sc} on the light intensity ($J \propto I^{\alpha}$), which exhibits a linear relation on a double logarithmic scale. The fitted α values for all three PVSCs are 0.93–0.94. As reported, a solar cell with no space charge effect will have an α value close to 1.[58] Therefore, our PVSCs using SnO_2 ESLs and spiro-OMeTAD hole-selective layers do not appear to be mainly space charge limited. The improvement in the PCE after adding the $Pb(SCN)_2$ additive in the precursor should be due to the improved film quality such as enlarged grain size.

Figure 9a shows the stabilized PCEs of the $FAPbI_3$, $FA_{0.8}Cs_{0.2}PbI_3$, and $FA_{0.8}Cs_{0.2}PbI_3$+0.5% $Pb(SCN)_2$ PVSCs. It is clear that by 20% Cs substitution of FA, the stabilized PCE improves from 10.56% ($FAPbI_3$) to 14.67 ($FA_{0.8}Cs_{0.2}PbI_3$). By adding 0.5% $Pb(SCN)_2$, the stabilized PCE further improves to 17.65% [$FA_{0.8}Cs_{0.2}PbI_3$+0.5% $Pb(SCN)_2$]. It is also noted that the PCE curve of $FAPbI_3$ has a decreasing trend with respect to time, because $FAPbI_3$ is not stable against moisture, whereas the PCE curves of $FA_{0.8}Cs_{0.2}PbI_3$ and $FA_{0.8}Cs_{0.2}PbI_3$+0.5% $Pb(SCN)_2$ are rather flat. The reason is that Cs substitution improves the perovskite stability and the addition of $Pb(SCN)_2$ does not change this fact. The PVSCs were stored in a dry box under room light, and the *J–V* curves were measured daily in ambient air (25 °C, 50% humidity) over a 10 day period. The as-measured PCE versus storage time is shown in Figure 9b. The PCE (10 day) to PCE (0 day) ratios are 54.4, 93.7, and 96.5% for $FAPbI_3$, $FA_{0.8}Cs_{0.2}PbI_3$, and $FA_{0.8}Cs_{0.2}PbI_3$+0.5% $Pb(SCN)_2$, respectively. Therefore, we conclude that by Cs substitution and $Pb(SCN)_2$ addition, both a higher PCE and improved perovskite stability could be achieved for FA-based PVSCs.

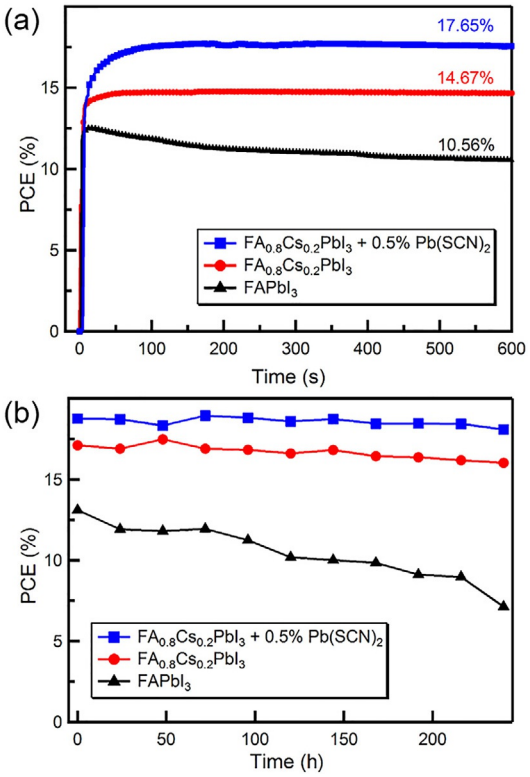

Figure 9. a) Stabilized PCE and b) PCE versus storage time of $FAPbI_3$ and $FA_{0.8}Cs_{0.2}PbI_3$ PVSCs with and without 0.5% $Pb(SCN)_2$ as additive, respectively.

Conclusions

We examined the main factors limiting the performance of formamidinium and cesium lead triiodide ($FA_{1-x}Cs_xPbI_3$) perovskite solar cells (PVSCs). We found that small grain sizes (≈120 nm) caused by Cs substitutions led to short carrier lifetimes, which limited the device performance. We also found that adding a small amount of $Pb(SCN)_2$ as an additive in the precursors could enlarge the grain size of $FA_{1-x}Cs_xPbI_3$ perovskite thin films and significantly increase the carrier lifetimes. With an optimal 0.5 mol% $Pb(SCN)_2$ additive, the average power conversion efficiency (PCE) was increased from 16.18±0.50 (13.45±0.78)% to 18.16±0.54 (16.86±0.63)% for planar $FA_{0.8}Cs_{0.2}PbI_3$ PVSCs measured under reverse (forward) voltage scans. The champion cell showed a PCE of 19.57 (18.12)%. This performance is now comparable with that of the best-performing methylammonium-containing planar FA-based lead halide PVSCs.[16,37]

Experimental Section

Thin-film fabrication

The perovskite thin films were deposited by using a process similar to that described in our earlier work.[48,49] The $FA_{1-x}Cs_xPbI_3$ (x=0, 0.05, 0.1, 0.15, 0.2, 0.25, 0.3) precursor solution was prepared by dissolving $CH(NH_2)_2I$ (1−x mmol; FAI, Dyesol), CsI (x mmol; Alfa Aesar, 99.9%) and PbI_2 (1 mmol; Alfa Aesar, 99.9985%) in *N*,*N*-dimethylformamide (DMF)/dimethyl sulfoxide (DMSO) (3:1, 1 mL). The perovskite thin films were spin coated on the electron-selective layers (ESLs) at 4000 rpm for 60 s with diethyl ether (750 μL; Alfa Aesar, 99%) dripped simultaneously during the spinning. $FA_{1-x}Cs_xPbI_3$ (x=0, 0.05, 0.1) was annealed at 150 °C for 10 min, whereas $FA_{1-x}Cs_xPbI_3$ (x=0.15, 0.2, 0.25, 0.3) was annealed at 100 °C for 10 min. The $FA_{0.8}Cs_{0.2}PbI_3$ precursor solution with $Pb(SCN)_2$ (Sigma–Aldrich, 99.5%) was prepared by adding an additional amount of $Pb(SCN)_2$ (0, 0.25, 0.5, 1, 1.5, 2 mol% with respect to PbI_2) to the aforementioned solution. All chemicals used in this work were commercially available and were used as received.

Device fabrication

Fluorine-doped tin oxide (FTO) glass (Pilkington, NSG TEC-15) was used as the substrate and was cleaned by sequential ultrasonication in diluted Micro-90 detergent, deionized water, acetone, and isopropyl alcohol each for 15 min and was then blow-dried with nitrogen gas. The SnO_2 ESLs were deposited by plasma-enhanced atomic layer deposition (ALD, Ensure Scientific Group AutoALD-PE V2.0) following the process described in our earlier work.[48] Tetrakis(dimethylamino)tin(IV) (99%, Strem Chemicals Inc.) was used as the tin precursor and was held at 75 °C, whereas pure oxygen gas was used as the oxidizer. SnO_2 was deposited at 100 °C and was UV ozone treated for 10 min before depositing the next layer.

A C_{60}-SAM (self-assembled momnolayer) was applied to passivate the ESLs. First, a C_{60}-SAM solution was prepared in cholorobenzene (CB, Sigma–Aldrich, 99.8%) with vigorous stirring overnight. C_{60}-SAM was then deposited by spin coating following reports in literature.[48,59] The perovskite absorber layers were deposited on the ESLs by using the aforementioned process. The hole-selective layers (HSLs) were prepared by spin coating the HSL solution at 2500 rpm for 60 s. The HSL solution was prepared by dissolving spiro-OMeTAD (68 mmol; Shenzhen Feiming Science and Technology Co., Ltd., 99.0%), lithium bis(trifluoromethanesulfonyl)imide (LiTFSI, 26 mmol, Sigma, 99.95%), and 4-*tert*-butylpyridine (TBP, 55 mmol, Sigma, 96%) in a mixed solvent of and acetonitrile (Sigma, 99.8%) (10:1 v/v, 1 mL). Finally, 80 nm gold (Au) was thermally evaporated through a metal mask on the HSLs. The finished device had the regular architecture of FTO/SnO_2/C_{60}-SAM/$FA_{0.8}Cs_{0.2}PbI_3$/spiro-OMeTAD/Au and the active area was 0.08 cm^2.

Thin-film characterization

Scanning electron microscopy (SEM) images were taken with a Hitachi S-4800 high-resolution microscope. Atomic force microscopy (AFM) images were recorded with a Veeco Nanoscope V instrument. The structural properties were characterized by measurement and analysis of the X-ray diffraction (XRD) patterns acquired with a Rigaku Ultima III high-resolution X-ray diffractometer by using the CuK_α line ($\lambda = 0.154$ nm) at 44 kV and 40 mA source excitation. Absorbance spectra were obtained with a UV/Vis spectrophotometer (PerkinElmer Lambda 1050). PL measurements were conducted in air at room temperature. Samples were illuminated from the film side. A 532 nm cw laser (beam diameter $\approx$88 μm) at 21 mW cm^{-2} was used as the source of excitation for PL measurements. PL signal was detected by a Symphony-II CCD (from Horiba) detector after a 300 g mm^{-1} grating monochromator (integration time = 0.1 s). For TRPL, the excitation wavelength was a 532 nm pulsed laser (beam diameter $\approx$150 μm). TRPL was performed with time-correlated single-photon counting (TCSPC) module (Becker & Hickel Simple Tau SPCM 130-E/M module) and the PL signal was collected (Integration time = 600 s) by a hybrid APD/PMT module (R10467U-50).

Device characterization

J–V curves were measured by using a Keithley2400 sourcemeter, with the samples under AM1.5G (100 W cm^{-2}) illumination (PV Measurements Inc.), the potential of which swept between −0.5 and 2 V with a voltage settling time of 10 ms. EQE spectra were measured by using a commercialized QE system (PV Measurements Inc.), the monochromatic light intensity of which was calibrated with a standard silicon diode at each wavelength. All device characterizations were performed in ambient air (25 °C, 50% humidity).

Acknowledgements

This work was financially supported by the U.S. Department of Energy (DOE) SunShot Initiative under the Next Generation Photovoltaics 3 program (DE-FOA-0000990), National Science Foundation under contract no. CHE-1230246 and DMR-1534686, and the Ohio Research Scholar Program. J.C. thanks the financial support from National Natural Science Foundation Project of China (61674029).

Keywords: cesium · energy conversion · perovskite · renewable resources · solar cells

[1] A. Kojima, K. Teshima, Y. Shirai, T. Miyasaka, *J. Am. Chem. Soc.* **2009**, *131*, 6050 – 6051.
[2] H.-S. Kim, C.-R. Lee, J.-H. Im, K.-B. Lee, T. Moehl, A. Marchioro, S.-J. Moon, R. Humphry-Baker, J.-H. Yum, J. E. Moser, M. Grätzel, N.-G. Park, *Sci. Rep.* **2012**, *2*, 591.
[3] M. M. Lee, J. Teuscher, T. Miyasaka, T. N. Murakami, H. J. Snaith, *Science* **2012**, *338*, 643 – 647.
[4] M. Liu, M. B. Johnston, H. J. Snaith, *Nature* **2013**, *501*, 395 – 398.
[5] J. Burschka, N. Pellet, S.-J. Moon, R. Humphry-Baker, P. Gao, M. K. Nazeeruddin, M. Grätzel, *Nature* **2013**, *499*, 316 – 319.
[6] P.-W. Liang, C.-Y. Liao, C.-C. Chueh, F. Zuo, S. T. Williams, X.-K. Xin, J. Lin, A. K. Y. Jen, *Adv. Mater.* **2014**, *26*, 3748 – 3754.
[7] W.-J. Yin, T. Shi, Y. Yan, *Adv. Mater.* **2014**, *26*, 4653 – 4658.
[8] H. Zhou, Q. Chen, G. Li, S. Luo, T.-b. Song, H.-S. Duan, Z. Hong, J. You, Y. Liu, Y. Yang, *Science* **2014**, *345*, 542 – 546.
[9] M. A. Green, A. Ho-Baillie, H. J. Snaith, *Nat. Photonics* **2014**, *8*, 506 – 514.
[10] N. J. Jeon, J. H. Noh, Y. C. Kim, W. S. Yang, S. Ryu, S. I. Seok, *Nat. Mater.* **2014**, *13*, 897 – 903.
[11] W. Nie, H. Tsai, R. Asadpour, J.-C. Blancon, A. J. Neukirch, G. Gupta, J. J. Crochet, M. Chhowalla, S. Tretiak, M. A. Alam, H.-L. Wang, A. D. Mohite, *Science* **2015**, *347*, 522 – 525.
[12] J. Yang, B. D. Siempelkamp, D. Liu, T. L. Kelly, *ACS Nano* **2015**, *9*, 1955 – 1963.
[13] J. You, L. Meng, T.-B. Song, T.-F. Guo, Y. Yang, W.-H. Chang, Z. Hong, H. Chen, H. Zhou, Q. Chen, Y. Liu, N. De Marco, Y. Yang, *Nat. Nanotechnol.* **2016**, *11*, 75 – 81.
[14] Y. Shao, Y. Yuan, J. Huang, *Nat. Energy* **2016**, *1*, 15001.
[15] X. Li, D. Bi, C. Yi, J.-D. Décoppet, J. Luo, S. M. Zakeeruddin, A. Hagfeldt, M. Grätzel, *Science* **2016**, *353*, 58 – 62.
[16] D. P. McMeekin, G. Sadoughi, W. Rehman, G. E. Eperon, M. Saliba, M. T. Hörantner, A. Haghighirad, N. Sakai, L. Korte, B. Rech, M. B. Johnston, L. M. Herz, H. J. Snaith, *Science* **2016**, *351*, 151 – 155.
[17] NREL Best Research-Cell Efficiencies Chart, http://www.nrel.gov/ncpv/images/efficiency_chart.jpg, accessed July 2016.
[18] W. Shockley, W. T. Read, *Phys. Rev.* **1952**, *87*, 835 – 842.
[19] J. H. Noh, S. H. Im, J. H. Heo, T. N. Mandal, S. I. Seok, *Nano Lett.* **2013**, *13*, 1764 – 1769.
[20] J. A. Christians, P. A. Miranda Herrera, P. V. Kamat, *J. Am. Chem. Soc.* **2015**, *137*, 1530 – 1538.
[21] S. N. Habisreutinger, T. Leijtens, G. E. Eperon, S. D. Stranks, R. J. Nicholas, H. J. Snaith, *Nano Lett.* **2014**, *14*, 5561 – 5568.
[22] J.-W. Lee, D.-J. Seol, A.-N. Cho, N.-G. Park, *Adv. Mater.* **2014**, *26*, 4991 – 4998.
[23] B. Hailegnaw, S. Kirmayer, E. Edri, G. Hodes, D. Cahen, *J. Phys. Chem. Lett.* **2015**, *6*, 1543 – 1547.
[24] C. C. Stoumpos, C. D. Malliakas, M. G. Kanatzidis, *Inorg. Chem.* **2013**, *52*, 9019 – 9038.
[25] R. K. Misra, S. Aharon, B. Li, D. Mogilyansky, I. Visoly-Fisher, L. Etgar, E. A. Katz, *J. Phys. Chem. Lett.* **2015**, *6*, 326 – 330.
[26] B. Conings, J. Drijkoningen, N. Gauquelin, A. Babayigit, J. D'Haen, L. D'Olieslaeger, A. Ethirajan, J. Verbeeck, J. Manca, E. Mosconi, F. De Angelis, H.-G. Boyen, *Adv. Energy Mater.* **2015**, *5*, 1500477.
[27] G. E. Eperon, S. D. Stranks, C. Menelaou, M. B. Johnston, L. M. Herz, H. J. Snaith, *Energy Environ. Sci.* **2014**, *7*, 982 – 988.
[28] S. Aharon, A. Dymshits, A. Rotem, L. Etgar, *J. Mater. Chem. A* **2015**, *3*, 9171 – 9178.
[29] F. Wang, H. Yu, H. Xu, N. Zhao, *Adv. Funct. Mater.* **2015**, *25*, 1120 – 1126.
[30] S. Pang, H. Hu, J. Zhang, S. Lv, Y. Yu, F. Wei, T. Qin, H. Xu, Z. Liu, G. Cui, *Chem. Mater.* **2014**, *26*, 1485 – 1491.
[31] J.-W. Lee, S. H. Lee, H.-S. Ko, J. Kwon, J. H. Park, S. M. Kang, N. Ahn, M. Choi, J. K. Kim, N.-G. Park, *J. Mater. Chem. A* **2015**, *3*, 9179 – 9186.
[32] D.-J. Seol, J.-W. Lee, N.-G. Park, *ChemSusChem* **2015**, *8*, 2414 – 2419.
[33] Z. Li, M. Yang, J.-S. Park, S.-H. Wei, J. J. Berry, K. Zhu, *Chem. Mater.* **2016**, *28*, 284 – 292.
[34] G. Kieslich, S. Sun, A. K. Cheetham, *Chem. Sci.* **2014**, *5*, 4712 – 4715.
[35] C. C. Stoumpos, M. G. Kanatzidis, *Acc. Chem. Res.* **2015**, *48*, 2791 – 2802.

[36] C. Yi, J. Luo, S. Meloni, A. Boziki, N. Ashari-Astani, C. Grätzel, S. M. Zakeeruddin, U. Rothlisberger, M. Grätzel, *Energy Environ. Sci.* **2016**, *9*, 656 – 662.
[37] M. Saliba, T. Matsui, J.-Y. Seo, K. Domanski, J.-P. Correa-Baena, M. K. Nazeeruddin, S. M. Zakeeruddin, W. Tress, A. Abate, A. Hagfeldt, M. Grätzel, *Energy Environ. Sci.* **2016**, *9*, 1989 – 1997.
[38] J.-W. Lee, D.-H. Kim, H.-S. Kim, S.-W. Seo, S. M. Cho, N.-G. Park, *Adv. Energy Mater.* **2015**, *5*, 1501310.
[39] S. Wozny, M. Yang, A. M. Nardes, C. C. Mercado, S. Ferrere, M. O. Reese, W. Zhou, K. Zhu, *Chem. Mater.* **2015**, *27*, 4814 – 4820.
[40] N. J. Jeon, J. H. Noh, W. S. Yang, Y. C. Kim, S. Ryu, J. Seo, S. I. Seok, *Nature* **2015**, *517*, 476 – 480.
[41] W. Travis, E. N. K. Glover, H. Bronstein, D. O. Scanlon, R. G. Palgrave, *Chem. Sci.* **2016**, *7*, 4548 – 4556.
[42] N. Pellet, P. Gao, G. Gregori, T. Y. Yang, M. K. Nazeeruddin, J. Maier, M. Grätzel, *Angew. Chem. Int. Ed.* **2014**, *53*, 3151 – 3157; *Angew. Chem.* **2014**, *126*, 3215 – 3221.
[43] W. S. Yang, J. H. Noh, N. J. Jeon, Y. C. Kim, S. Ryu, J. Seo, S. I. Seok, *Science* **2015**, *348*, 1234 – 1237.
[44] B. Xu, D. Bi, Y. Hua, P. Liu, M. Cheng, M. Grätzel, L. Kloo, A. Hagfeldt, L. Sun, *Energy Environ. Sci.* **2016**, *9*, 873 – 877.
[45] M. Saliba, S. Orlandi, T. Matsui, S. Aghazada, M. Cavazzini, J.-P. Correa-Baena, P. Gao, R. Scopelliti, E. Mosconi, K.-H. Dahmen, *Nat. Energy* **2016**, *1*, 15017.
[46] E. Zimmermann, K. K. Wong, M. Müller, H. Hu, P. Ehrenreich, M. Kohlstädt, U. Würfel, S. Mastroianni, G. Mathiazhagan, A. Hinsch, T. P. Gujar, M. Thelakkat, T. Pfadler, L. Schmidt-Mende, *APL Materials* **2016**, *4*, 091901.
[47] W. Ke, G. Fang, Q. Liu, L. Xiong, P. Qin, H. Tao, J. Wang, H. Lei, B. Li, J. Wan, *J. Am. Chem. Soc.* **2015**, *137*, 6730 – 6733.
[48] C. Wang, D. Zhao, C. Grice, W. Liao, Y. Yu, A. Cimaroli, N. Shrestha, P. J. Roland, J. Chen, Z. Yu, P. Liu, N. Cheng, R. Ellingson, X. Zhao, Y. Yan, *J. Mater. Chem. A* **2016**, *4*, 12080.
[49] W. Ke, C. Xiao, C. Wang, B. Saparov, H.-S. Duan, D. Zhao, Z. Xiao, P. Schulz, S. P. Harvey, W. Liao, W. Meng, Y. Yu, A. J. Cimaroli, C.-S. Jiang, K. Zhu, M. Al-Jassim, G. Fang, D. B. Mitzi, Y. Yan, *Adv. Mater.* **2016**, *28*, 5214 – 5221.
[50] Q. Jiang, D. Rebollar, J. Gong, E. L. Piacentino, C. Zheng, T. Xu, *Angew. Chem. Int. Ed.* **2015**, *54*, 7617 – 7620; *Angew. Chem.* **2015**, *127*, 7727 – 7730.
[51] M. Daub, H. Hillebrecht, *Angew. Chem. Int. Ed.* **2015**, *54*, 11016 – 11017; *Angew. Chem.* **2015**, *127*, 11168 – 11169.
[52] Z. Xiao, W. Meng, B. Saparov, H.-S. Duan, C. Wang, C. Feng, W. Liao, W. Ke, D. Zhao, J. Wang, D. B. Mitzi, Y. Yan, *J. Phys. Chem. Lett.* **2016**, *7*, 1213 – 1218.
[53] S. Yang, W. Liu, L. Zuo, X. Zhang, T. Ye, J. Chen, C.-Z. Li, G. Wu, H. Chen, *J. Mater. Chem. A* **2016**, *4*, 9430 – 9436.
[54] D. Zhao, M. Sexton, H.-Y. Park, G. Baure, J. C. Nino, F. So, *Adv. Energy Mater.* **2015**, *5*, 1401855.
[55] Y.-K. Wang, Z.-C. Yuan, G.-Z. Shi, Y.-X. Li, Q. Li, F. Hui, B.-Q. Sun, Z.-Q. Jiang, L.-S. Liao, *Adv. Funct. Mater.* **2016**, *26*, 1375 – 1381.
[56] J. Pan, C. Mu, Q. Li, W. Li, D. Ma, D. Xu, *Adv. Mater.* **2016**, *28*, 8309 – 8314.
[57] D. Zhao, W. Ke, C. R. Grice, A. J. Cimaroli, X. Tan, M. Yang, R. W. Collins, H. Zhang, K. Zhu, Y. Yan, *Nano Energy* **2016**, *19*, 88 – 97.
[58] V. D. Mihailetchi, J. Wildeman, P. W. M. Blom, *Phys. Rev. Lett.* **2005**, *94*, 126602.
[59] X. Liu, K.-W. Tsai, Z. Zhu, Y. Sun, C.-C. Chueh, A. K. Y. Jen, *Adv. Mater. Interfaces* **2016**, *3*, 1600122.

Received: July 28, 2016
Published online on October 26, 2016